Biosurface and Biotribology

WILEY

The Institution of Engineering and Technology

ORIGINAL RESEARCH OPEN ACCESS

Multi-Scale Strain-Friction Mapping in Human Finger Pads Using 3D-Digital Image Correlation and Optical Coherence Tomography

Zing Siang Lee[1,2] | Raman Maiti[3] | Matt Carré[2] | Roger Lewis[2]

[1]Robotics Institute, Ningbo University of Technology, Ningbo, China | [2]School of Mechanical, Aerospace and Civil Engineering, University of Sheffield, Sheffield, UK | [3]School of Mechanical, Electrical and Manufacturing Engineering, Loughborough University, Loughborough, UK

Correspondence: Zing Siang Lee (zslee@nbut.edu.cn; zing.siang.lee@sheffield.ac.uk)

Received: 19 June 2025 | **Revised:** 10 February 2026 | **Accepted:** 21 March 2026

Keywords: digital image correlation | finger-pad tribology | friction | optical coherence tomography | surface strain

ABSTRACT

Finger pad strain governs grip control and tactile feedback, yet in vivo measurements during sliding remain scarce. This feasibility study utilised 3D-digital image correlation (3D-DIC) and optical coherence tomography (OCT) for quantifying surface strains and subsurface deformation in a human finger pad during static/dynamic glass contact, linking both to the respective friction behaviour. Principal strains increase systematically with normal load (0.5–3 N), concentrating at the mechanoreceptor-rich fingertip under dynamic sliding (peak ε_1 2%–7.5%). Friction (CoF 0.4–0.8) and apparent contact area follow load-dependent power laws, with adhesion dominating. Multiscale imaging validates surface strain as a reliable friction predictor, providing good proof-of-concept for strain-based human finger pad friction modelling despite subsurface measurement limitations.

1 | Introduction

Hands and fingers enable precise gripping and manipulation through the viscoelastic properties of human skin, which readily deforms upon contact with diverse materials. Although excessive strain risks discomfort or damage (bruises, grazes and cuts), experimental measurements of finger pad strain during contact remain sparse. Recent advances are addressing this gap, Delhaye et al. [1] quantified skin strains to elucidate tactile sensory mechanisms, whereas Delhaye et al. [2] showed rapid grip force adaptation to changing friction depends on localised finger pad strains. These demonstrate that critical role of strain dynamics in grip control and tactile feedback.

Human skin friction is comparatively well-characterised and studied, normally influenced by skin condition, surface properties, material pairing, hydration, lipid films, trapped intermediates, ageing and gender [3–8]. Adhesion and deformation typically dominate interaction mechanisms [9–11]. Recent work by Li et al. [12] modelled and experimentally validated texture and direction dependent finger friction, identifying real contact area and adhesion variations as key drivers. Similarly, Nakanishi et al. [13] examined index finger friction and tactile perception on textured glass during swipes, revealing the combined influence of surface texture and motion dynamics. In addition, Zhou et al. [14] reviewed devices for active/passive tactile friction measurement, highlighting needs for precision, repeatability and advanced signal processing to quantify force fluctuations and perceptual accuracy in fingertip experiments. Although strain was not measured in these studies, it must have contributed substantially to the observed friction and perceptual responses.

As such, this study aimed to bridge strain and friction of the human finger pad, extending from the finger pad simulant work [15] that only examined the bulk strain of a synthetic finger pad simulant. The bulk finger pad strain and localised deformation during sliding contact with smooth optical glass substrate were visualised using 3D digital image correlation (DIC) and optical coherence tomography (OCT), respectively. These complementary imaging modalities reveal the strain-friction interplay at the skin-material interface, advancing understanding of grip performance and tactile sensation.

2 | Methodology

2.1 | Experimental Protocols

The left finger pad of a single healthy male volunteer (age 25) was used in this feasibility study. A single participant was selected to establish proof-of-concept for the proposed measurement method, enabling focused validation of the experimental protocol before scaling to a multisubject study.

The finger pad was pressed against a thin optical glass substrate (average thickness 396 μm) as shown in the experimental set-up in Figure 1. This glass thickness optimised OCT imaging quality during sliding tests by minimising internal reflections inherent to the material's high reflectivity, which could otherwise overlay afterimages and degrade scanned images of the subsurface finger pad structure.

Ambient conditions at the respective test sites were 26.6°C/36%–37% RH (3D-DIC) and 20.0°C/45%–50% RH (OCT), reflecting the fixed laboratory environments where each imaging modality was housed. Interaction forces were recorded using a 6-axis HE6 × 6 force plate (AMTI, USA). Normal loads targeted at 0.5 N, 1 N, 2 N and 3 N (within the low-load regime of the double-stage shear force model) were applied and stabilised before dragging the glass plate against the finger pad at a constant speed of 0.26 mm/s. Plate motion was controlled via LabVIEW software on the test rig. The study protocol was approved by The University of Sheffield (Ethics Number 002074).

Each test condition was performed once without repetition. The study's objective was focused on demonstrating feasibility of linking strain and friction measurements using both 3D-DIC and OCT imaging modalities. As such, 3D-DIC generated four datasets corresponding to the four normal load conditions, whereas OCT produced eight datasets from imaging two distinct localised regions under each load. This difference reflects imaging targets rather than repeats: 3D-DIC captured bulk contact area surface strain (one region per condition), whereas OCT imaged two separate locations spanning the longest cross-section of the contact region. Single measurements per condition proved sufficient to establish method feasibility.

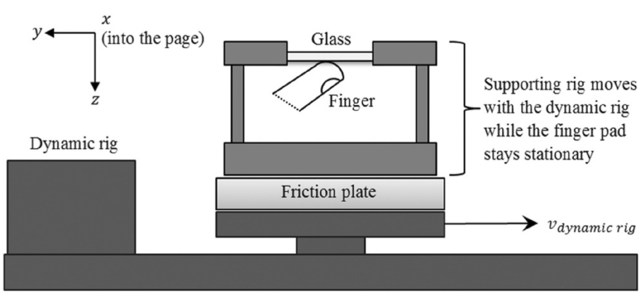

FIGURE 1 | Illustration of the finger pad sliding experiment set-up.

2.2 | 3D-Digital Image Correlation (3D-DIC)

DIC is an optical numerical full-field measuring technique that can compute field of displacement or surface strain of the experimental object through comparison of images of undeformed and deformed specimens. The working principle of DIC relies on the tracking of random and unique speckle patterns on the material surface as shown in Figure 2a. A DIC system that uses one camera is 2D-DIC and two cameras is 3D-DIC. Both systems have the same working principle.

Using a 3D-DIC system requires careful sample preparation, camera set-up and calibration, acquisition of images and post-analysis [16, 17]. Droplets of black water-based ink (crafters acrylic paint, DecoArt Inc., Stanford) were distributed randomly on the finger pad by flicking the bristles of a toothbrush and then left to dry for approximately 2–4 min before the friction and 3D-DIC testing. Setting up the camera required adjustment of the stereo angle of the cameras and the distance between the cameras, as shown in Figure 3, which were set at 30° and 150 mm respectively. Two Pike F505B cameras (Allied Vision Technologies GmbH, Germany) equipped with monochromatic CCD sensor (Sony ICX625; 2/3″; 2452 × 2054 pixels) and 50 mm lens objectives (XENOPLAN2.8/50-0902, Schneider, Kreuznach) were used. After setting-up the cameras, they were calibrated with a known grid size pattern of 11 × 10 with 2 mm spatial distance (calibration score: 0.062 pixels) by using VIC-3D digital image correlation software (version 7.2.1, Correlated Solutions, USA). The spatial pixel resolution was 0.013 mm/pixel, which would result in a field of view of approximately 33 × 27 mm^2 and an in-plane resolution of 0.009 mm^2. The image acquisition stage started before the finger pad was in contact with the glass plate. Five pairs of images were captured every second throughout the sliding experiment. Due to a relatively large speckle size, a subset size of 61 × 61 pixels was chosen for the correlation of images as shown in Figure 2b. The step size and the filter size were 7 and 15, respectively. The strain data were computed using Lagrange strain because the displacement is described by the material surface coordinates. The noise levels of the principal strain data were approximately 0.3%–0.4%. Details of the strain computation are explained in a previous study by Maiti et al. [18].

2.3 | Optical Coherence Tomography (OCT)

Optical coherence tomography (OCT) is a noninvasive imaging technique that can provide the surface and subsurface morphology of biological tissues. Vivosight OCT (Michelson Diagnostics, Kent) was used to visualise the interaction between the finger pad and the glass plate. A B-scan [19] was used because this could capture the cross-sectional image of the finger pad in real-time. The OCT set-up used in this study, as shown in Figure 4a, was the same as that used in a study by Maiti et al. [18]. The image capturing rate of a B-scan is 20 frames per second and the resolution of each image is

FIGURE 2 | (a) Finger pad with the applied speckles and (b) a magnified image showing an example speckle subset.

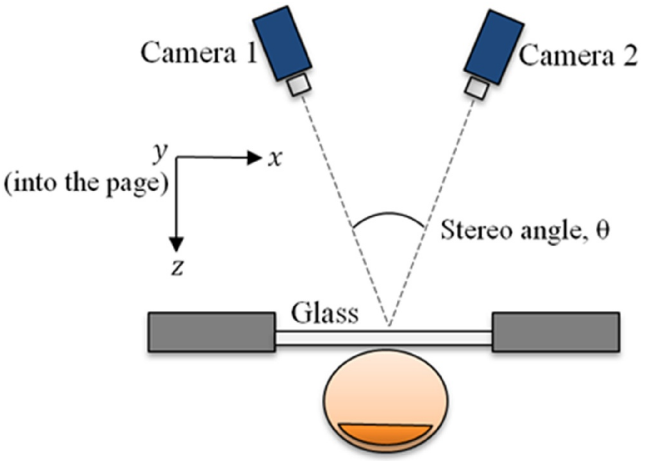

FIGURE 3 | Illustration of the experimental set-up for 3D-DIC experiments.

1342 × 460 pixels. For stability, the handheld probe was fixed on a microscope stand that also allowed position adjustment.

In the combined OCT-friction experiments, images were acquired at two distinct positions along the finger pad, as illustrated in Figure 4b, to capture the complete longitudinal cross-section of the contact region. For each position, B-scan OCT imaging commenced as the finger pad approached the glass plate. The finger pad was then pressed against the plate under controlled normal load and slid at constant speed until motion ceased. OCT scanning continued throughout the full sequence and concluded after the finger pad was retracted from the plate. This protocol enabled comprehensive visualisation of surface and subsurface deformation across the primary loading axis.

2.4 | Contact Area Computation

VIC-3D digital image correlation software (version 7.2.1, Correlated Solutions, USA) was used to generate the strain maps of the finger pad. Beyond strain analysis, it provided full-field point positions and displacement data for the speckled surface. As such, apparent contact area between the finger pad and glass plate could be estimated from the geometry profiles extracted from the DIC point cloud data. A bespoke MATLAB algorithm (developed at the University of Sheffield) identified boundary positions, shown as blue dots in Figure 5a, from the deformed finger pad geometry during contact. The dashed lines in Figure 5a reflect the geometry profile of a flattened finger pad shown in Figure 5b.

The algorithm detected boundary coordinates by analysing the changes in surface gradient across 100 cross-sectional profiles, spaced at 0.15 mm intervals. An ellipse best-fit function was then applied to these boundary coordinates to compute apparent contact area of the finger pad.

Real-apparent contact ratios were computed from OCT images to quantify ridge-level contact, providing insight into real versus apparent contact areas given the finger pad's papillary ridge structure. As ridges remain partially uncompressed against the glass plate, contact is incomplete. Following Liu et al. [20], the real-apparent contact ratio was calculated as below, where d_{real} is the total length of ridge segments in contact and d_{apparent} is the nominal contact length (see Figure 6). In the figure, only three ridges contribute to contact. This method applies to both static and sliding conditions.

$$\text{Real} - \text{apparent contact area ratio} = \frac{d_{\text{real}}}{d_{\text{apparent}}} = \frac{d_1 + d_2 + d_3 + \cdots d_n}{d_{\text{apparent}}}$$

3 | Results

3.1 | General Force Behaviour Before, During and After Sliding

Figure 7 illustrates normal and friction force evolution on the finger pad before, during and after sliding contact with the glass plate. The time origin ($t = 0$s) marks the onset of plate motion, with all experiments standardised by fixed sliding distance and speed.

Normal force was first applied and stabilised prior to sliding, during which minimal friction force was recorded. Plate motion then initiated adhesion breakdown, and the interface transitioned to steady state sliding once full slip occurred. Dynamic CoF was established from the friction force plateau. Postsliding,

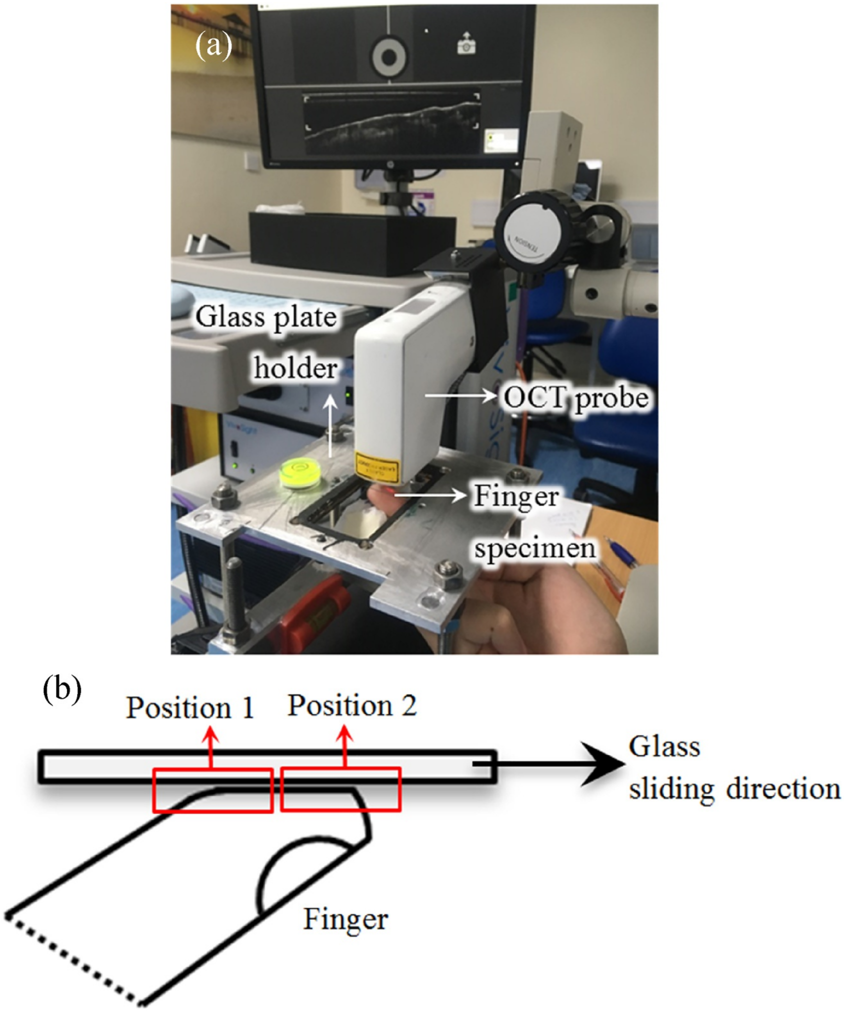

FIGURE 4 | (a) OCT experimental set-up and (b) the scanning positions of the OCT on the finger pad.

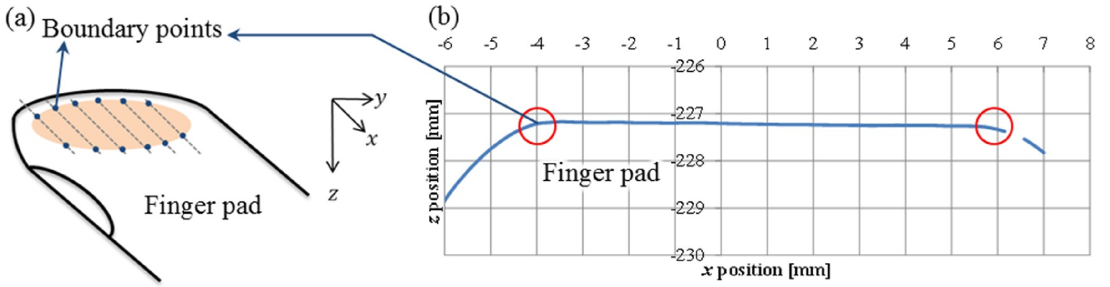

FIGURE 5 | (a) Illustration showing a flattened region of finger pad pressing against a flat plate (not shown) and the boundary points obtained from (b) the cross-sectional surface profile of the finger pad measured using 3D-DIC.

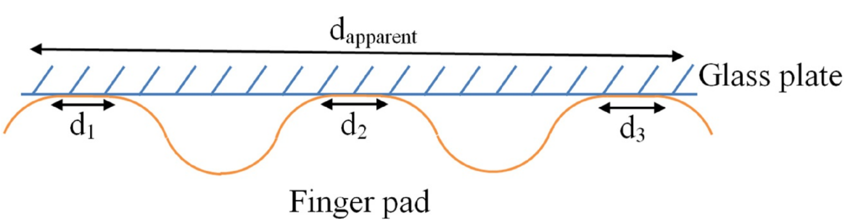

FIGURE 6 | Illustration of a finger pad loaded against a glass plate.

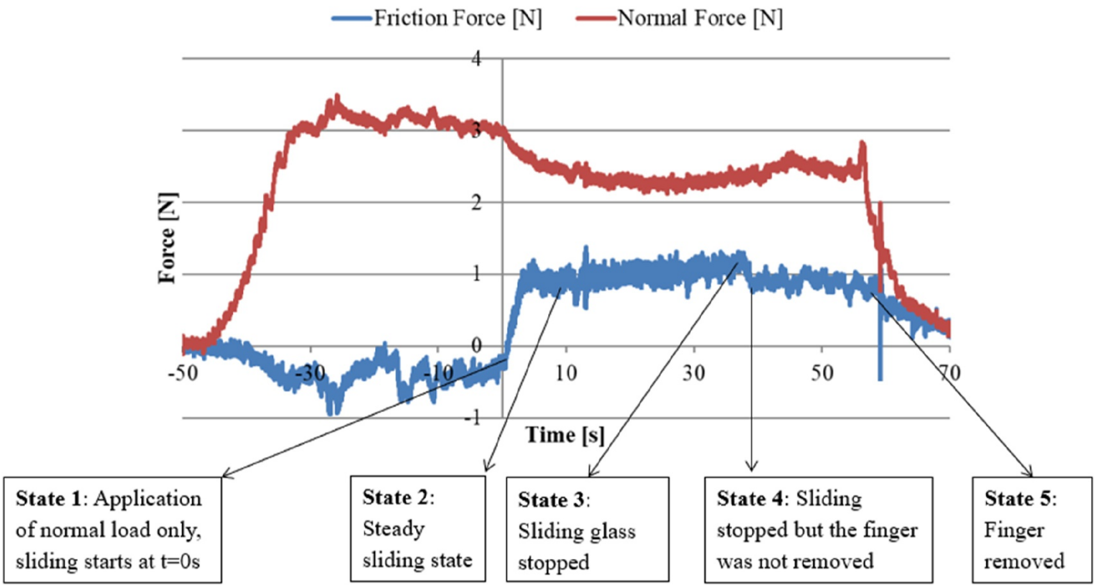

FIGURE 7 | Timeline of forces acting on a finger pad before, during and after sliding interaction, for a target normal load of 3 N.

the finger pad remained loaded briefly, exhibiting viscoelastic recovery as friction force decayed. The experiment concluded upon finger pad retraction.

Target normal loads were achieved presliding. However, normal force decreased immediately upon sliding onset, then recovered after a brief interval. This characteristic curved normal force profile during sliding was consistently observed across all tests in this study. Additionally, the curve amplitude scaled proportionally with the magnitude of the normal force. This behaviour resulted from the thin (396 μm thick) glass plate bending due to its relatively low stiffness under normal loading. Similar flexure was observed by Lee et al. [15] during synthetic finger pad tests. Thin optical glass substrate was used in this study to optimise OCT imaging clarity by minimising internal reflections and light distortion, enabling clear finger pad visualisation. The same thin geometry benefited 3D-DIC by reducing optical aberrations during surface strain measurement.

3.2 | Friction and Dynamic Coefficient of Friction

Figure 8a presents friction force versus normal load for both OCT and 3D-DIC experiments, whereas Figure 8b shows dynamic coefficient of friction (CoF) versus normal load. The dynamic CoF represents the average of instantaneous CoF values calculated over 20s of steady-state finger pad sliding, using concurrent normal and friction force measurements. The CoF inherent variation combined with a general decrease with increasing normal load observed in Figure 8b matches findings reported by Derler & Gerhardt [7]. A power-law regression was fitted to both friction force and dynamic CoF as functions of normal load and is shown in Figure 8a,b, respectively, together with the corresponding R^2 and p-values. A power-law model was selected because it has been widely adopted in previous studies [7, 20, 21]. The high R^2 for friction force indicates a very good relationship with normal load, whereas the dynamic CoF exhibits substantially more scatter and only a moderate trend. Where the p value is below 0.05, there is insufficient data to support a hypothesis that the relationship follows a power law. For some datasets, the relationships are strong and for others not. This may reflect random variation due to the relatively small number of tests performed. Friction forces and dynamic CoF measured during OCT experiments consistently exceeded those from 3D-DIC tests. This discrepancy reflects environmental differences between test locations (detailed in Methods Section 2.1), conducted on separate days with lower temperature and higher humidity conditions.

3.3 | General Surface Strain Behaviour

Figure 9b–e shows first principal strain ε_1 (tensile) and second principal strain ε_2 (compressive) on the finger pad surface under 0.5 N static loading. Figure 9a illustrates global coordinate axes and glass plate sliding direction relative to the stationary finger pad. Dashed white lines in the figures delineate the contact area boundary.

The transition to dynamic loading substantially alters both principal strain distributions. Negative first principal strain (ε_1) clusters in the fingertip region, see white arrows in Figure 9c, become more concentrated towards the fingertip. Second principal strain (ε_2) exhibits expanded negative coverage in the same distal region. This results in the palm-side periphery experiencing increased tensile loading, whereas the fingertip-side contact region becomes predominantly compressive. Skin proximal to the palm (outside contact) shows elevated strain in both principal strains, consistent with overall finger pad elongation from distal glass motion. Irregular strain fluctuations reflect both involuntary human motion artefacts and methodological factors, including experimental noise and software limitations in deformation/strain calculations.

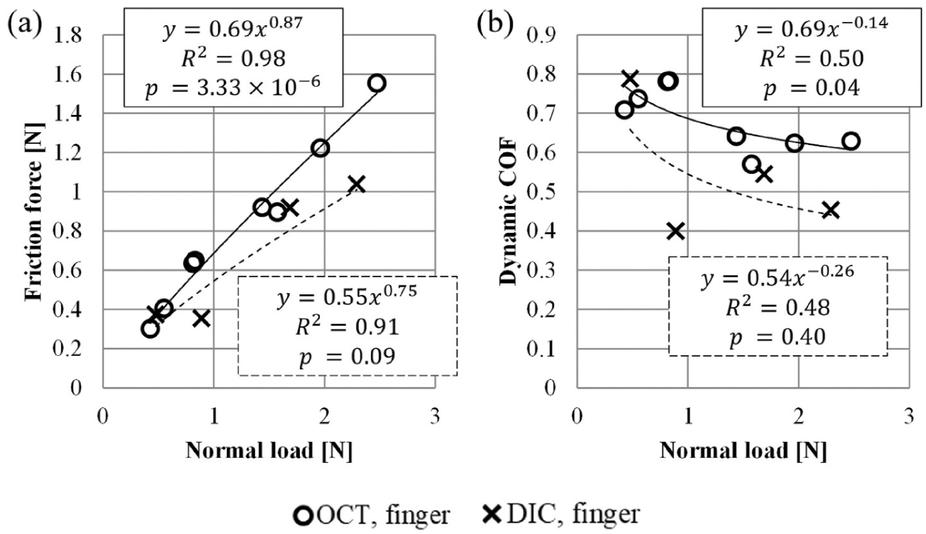

FIGURE 8 | (a) Friction force against normal load with (b) the dynamic coefficient of friction (COF) against normal load applied on the finger pad.

3.4 | Influence of the Normal Load on the Surface Strain Behaviour

Figure 10 presents cross-sectional surface strain profiles along the finger pad surface *y*-axis, illustrating normal load effects on strain distribution. Line profiles identify regional deformation tendencies, whereas Figure 11 shows mean contact area strains versus actual applied normal loads (noting lower dynamic vs. static values). Average contact strains provide quantitative finger pad response measures.

Static loading produces peak ε_1 at the palm-proximal contact edge, see black arrow in Figure 10a, increasing with normal load, alongside compressive ε_1 at the distal contact region. Dynamic loading retains this proximal peak, see Figure 10b, with modestly reduced magnitude, though overall proximal palm region strain increases. Distal compressive ε_1 remains largely unchanged. Mean ε_1 shows minimal static-to-dynamic differences, scaling consistently with load, as shown in Figure 11a,b.

Static ε_2 profiles exhibit flat low-amplitude waveforms, as seen in Figure 10c, except at 3 N where irregularity suggests motion artefact. Dynamic loading produces pronounced negative ε_2 peak at the fingertip-distal edge, see black arrow in Figure 10d, with peak magnitude decreasing at higher loads. Mean ε_2 shows no clear load relationship in either state as shown in Figure 11c,d.

3.5 | Contact Area and Contact Area Ratio

Figure 12a shows the apparent contact area of the finger pad increasing with normal load under static conditions, whereas Figure 12b depicts the same relationship under dynamic sliding conditions. A power-law regression was fitted in both figures, following the approach of Liu et al. [20]. The high R^2 indicates that changes in normal load explain nearly all variation in apparent contact area, with data points lying close to the fitted power-law curve. The associated *p* value of 0.01 confirms that this relationship is statistically significant at the 0.05 level.

The static contact areas fall within a similar range to those reported by Liu et al. [20], exhibiting rapid increases towards 100 mm^3 at low load. In contrast to Liu et al. [20], where dynamic apparent contact was consistently smaller than static, the static and dynamic trends in this study appear comparable across low load conditions, showing no pronounced decrease in dynamic contact area. This difference likely stems from the countererface: Liu et al. [20] used a thick rigid glass plate, whereas a thin optical glass substrate was employed in this study. This is discussed further in Section 4.8.

Figure 13a shows the real-apparent contact area ratio of the finger pad increasing gradually with normal load under static conditions, whereas Figure 13b reveals a similar trend under dynamic conditions, albeit with greater data scatter. Compared to the static real-apparent contact ratios reported by Liu et al. [20], the values in this study are substantially higher across the tested load range. A power-law regression was also fitted following the approach of Liu et al. [20]. The low R^2 (0.50 and 0.49) indicate that normal load explains only about half of the variation in dynamic coefficient of friction, with substantial scatter around the fitted power-law curves. The associated *p* value of 0.16 and 0.19 show that these trends are not statistically significant at the 0.05 level.

4 | Discussion

4.1 | Friction Mechanism

For the atomically smooth glass counterface used in this study (negligible surface roughness), adhesion dominates friction per Derler et al. [22]. The shallow negative slope of dynamic CoF versus normal load in Figure 8b confirms this mechanism, consistent with minimal hysteresis losses expected from low

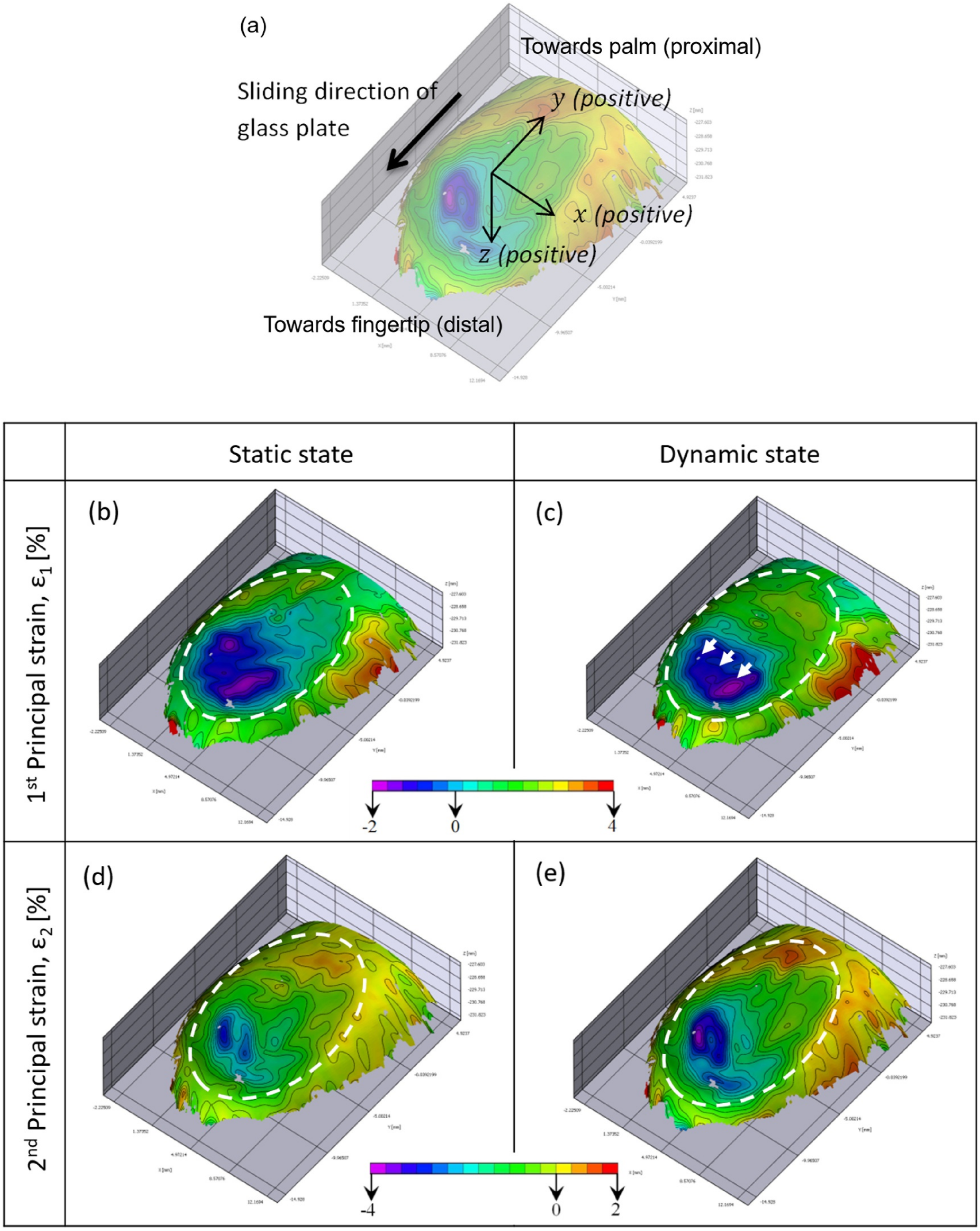

FIGURE 9 | (a) Global position axes used and the DIC results of the finger pad loaded at 0.5 N with the respective strains (b), (c) 1st principal strain ε_1 and (d), (e) 2nd principal strain ε_2.

viscoelastic deformation against such smooth substrates at low loads (< 3 N).

4.2 | Surface Strain Distribution Patterns

Palm-proximal contact regions exhibit elevated first principal strain, whereas fingertip-distal regions show higher second principal strain, when the plate slid in distal direction. Delhaye et al. [1] reported maximum values of both principal strains increasing with normal force during sliding, a trend confirmed here by peak strain value in Figure 10a,d. This reflects pronounced subsurface tissue deformation and contact pressure at higher loads.

Mean contact area strains were examined in this study to provide generalised metrics independent of contact geometry variations. Peak strains are sensitive to edge effects and contact

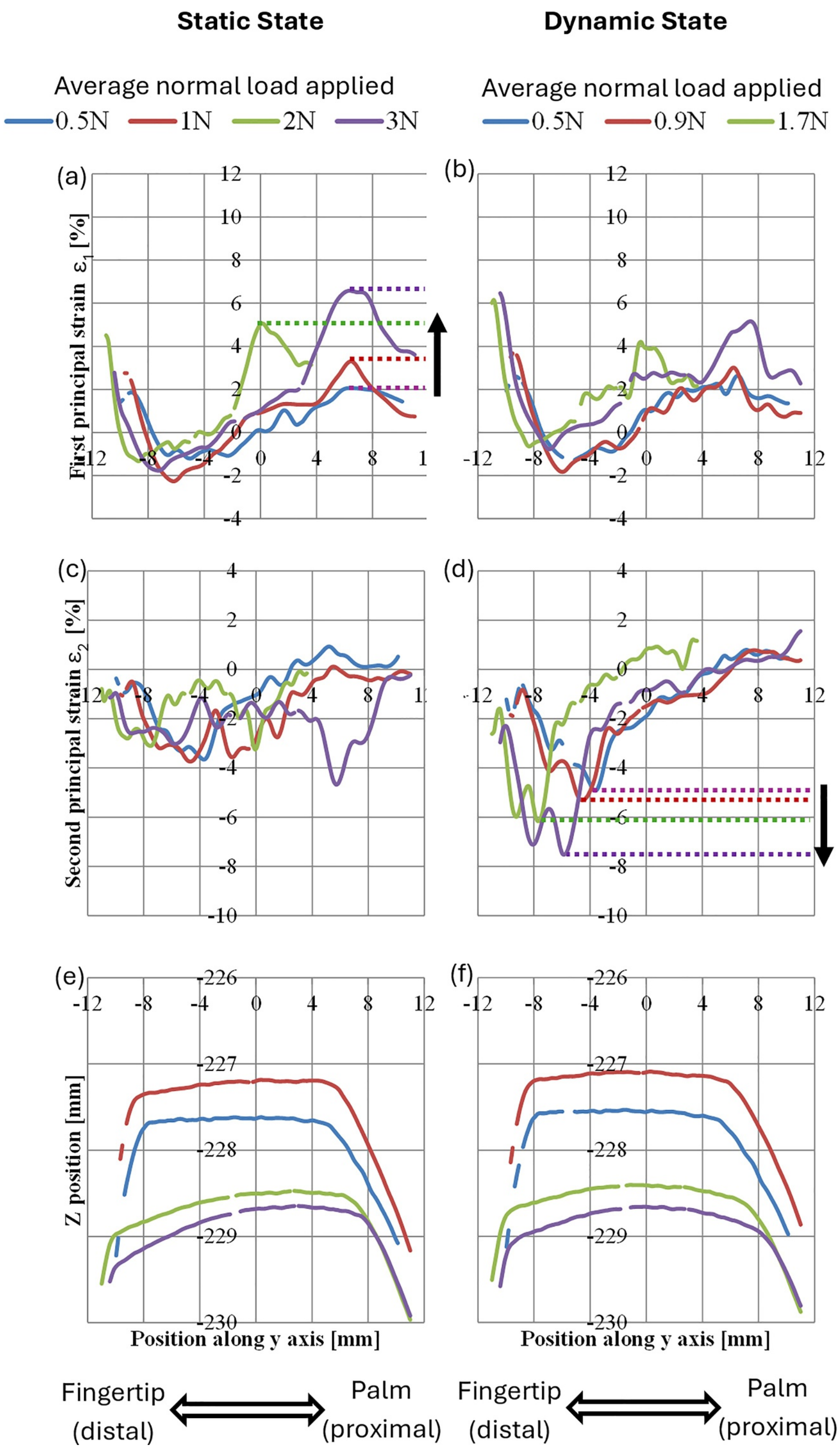

FIGURE 10 | First principal strain (ε_1) along the finger pad *y*-axis in (a) static and (b) dynamic states; second principal strain (ε_2) along the *y*-axis in (c) static and (d) dynamic states and finger pad geometry along the *y*-axis in (e) static and (f) dynamic states.

shape, whereas area-averaged values better represent bulk tissue response across different loading conditions. However, no clear static-dynamic distinctions emerge for either principal strain. First principal strain (ε_1) shows linear load dependence, consistent with progressive tensile stretching. On the other hand, second principal strain (ε_2) decreases rapidly with normal load then plateaus, suggesting compressive resistance saturates as stiffer deeper tissues engage. This limitation arises from the experimental rig, which could not apply lower normal loads to confirm the saturation behaviour. However, zero strain at zero normal load is physically expected as no deformation can occur without contact force.

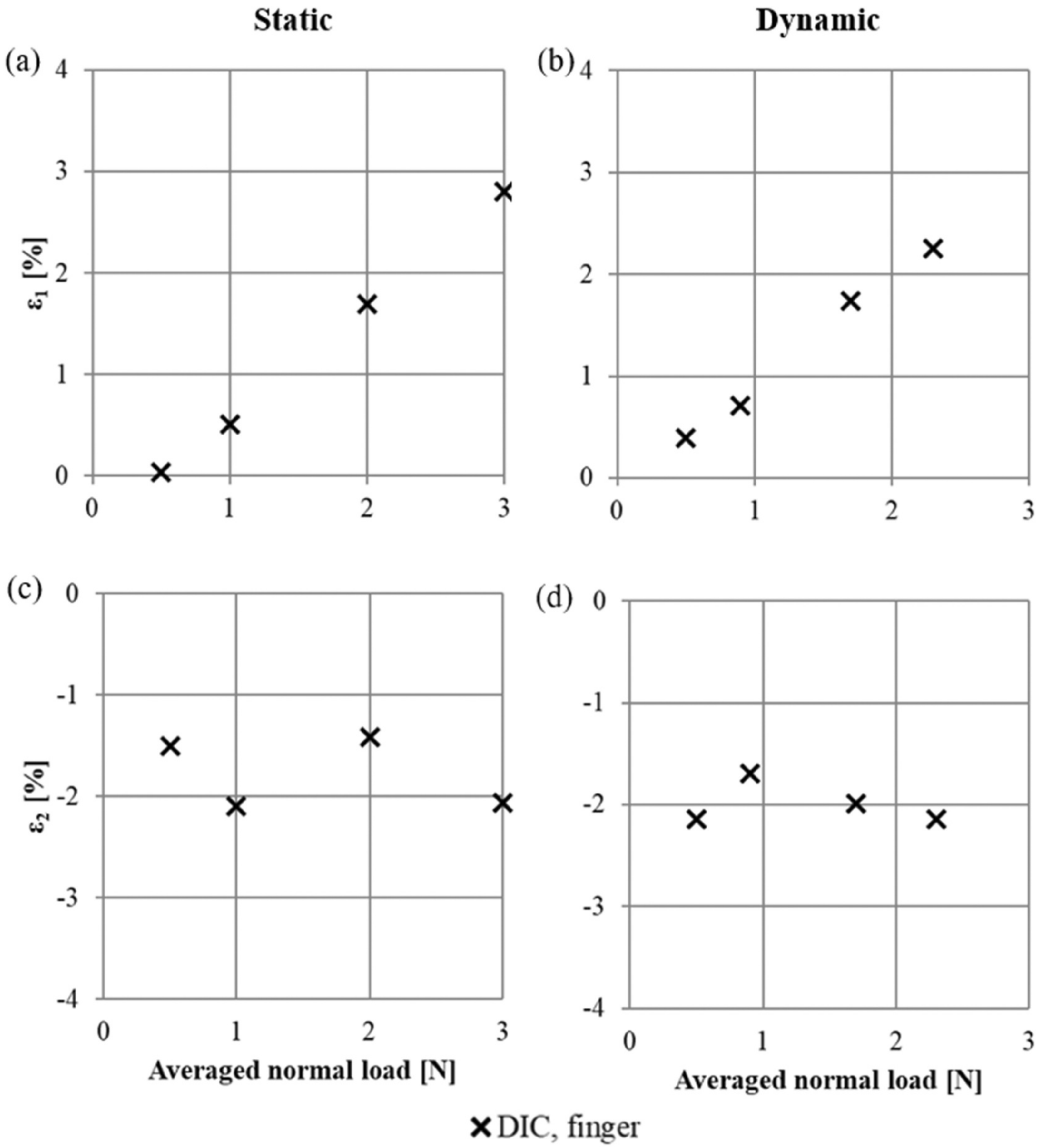

FIGURE 11 | Mean first principal strain ε_1 strain within the contact area of a finger pad from (a) static to (b) dynamic state, and mean second principal strain ε_2 strain within the contact area of the finger pad from (c) static to (d) dynamic state when plotted against the normal load applied to a finger pad.

4.3 | Surface Strain Magnitude Discrepancies

Reported peaked principal strains (2.0%–7.5%) in this study are substantially lower than the maximum principal strains of 25%–45% reported by Delhaye et al. [1]. Tests here also had reduced friction (CoF 0.4–0.8 vs. 1.0–2.0) which would contribute to the lower strain levels. The lower friction likely arose from a compound effect of sliding speed, ambient conditions and skin hydration.

Firstly, Delhaye et al. [1] used 2–20 mm/s sliding speeds versus 0.26 mm/s in this study. The slower rate allowed high-resolution imaging capture of deformation details, whilst allowing skin viscoelastic relaxation and thereby minimising strain amplification from rapid sliding and finger-plate adhesion. Secondly, Derler & Gerhardt [7] noted that temperature, humidity and skin hydration strongly modulate skin friction. This is evident in this study as OCT tests (20.0°C and 45%–50% RH) yielded higher CoF than DIC (26.6°C and 36%–37% RH), confirming environmental sensitivity. Although unreported in Delhaye et al. [1], the elevated friction and narrow maximum principal strain range across eight volunteers suggest more consistent skin hydration under conditions promoting higher friction, unlike the single drier participant in this study. Nevertheless, the single participant study still limits generalisation to broader populations as human skin properties vary significantly with age, gender, hydration and other factors [7, 23–25]. This proof-of-concept study establishes methodological feasibility, with multisubject validation planned for future work.

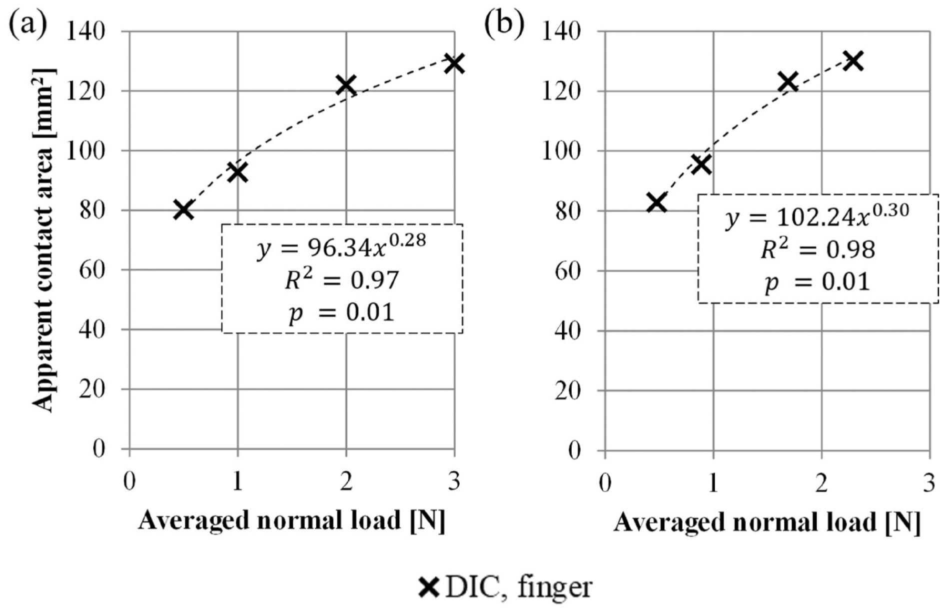

FIGURE 12 | The relationship between the apparent contact area and the normal load applied in (a) the static state and (b) the dynamic state.

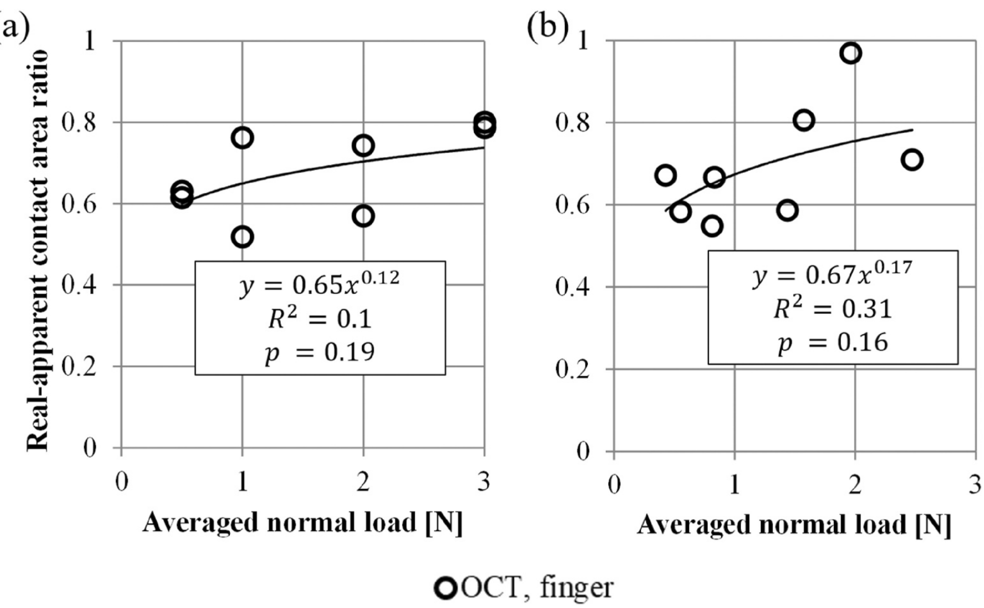

FIGURE 13 | The change of real apparent contact area ratio of the finger pad from (a) the static state to (b) the dynamic state with the average normal load.

4.4 | Localised Deformation of Finger Pad Ridges

3D-DIC can effectively visualise bulk strain across the entire finger pad contact area. However, it cannot resolve ridge-level deformation due to large speckle size, which limits the subset size (approximately 0.79 mm × 0.79 mm) to exceeding ridge spacing (approximately 0.5 mm in Figure 14). Additionally, camera resolution proved insufficient despite optimal optics calibration, as shown in Figure 2b, where DIC images failed to capture distinct finger pad ridges. Therefore, OCT was employed to capture localised finger pad deformation (see Figure 14), clearly showing finger pad ridge deformation as the plate transitions from initial contact to steady sliding. However, quantitative strain analysis using 3D-DIC software proved unsuccessful. OCT images lack distinctive speckle patterns due to uniform tissue texture and grayscale variation. Image quality was further compromised by light artsifacts (plate reflections) and noise, preventing reliable subset tracking.

4.5 | Strain-Friction Relationship

Within this study, both principal surface strains and friction coefficients (CoF) increase with normal load, driven by pronounced

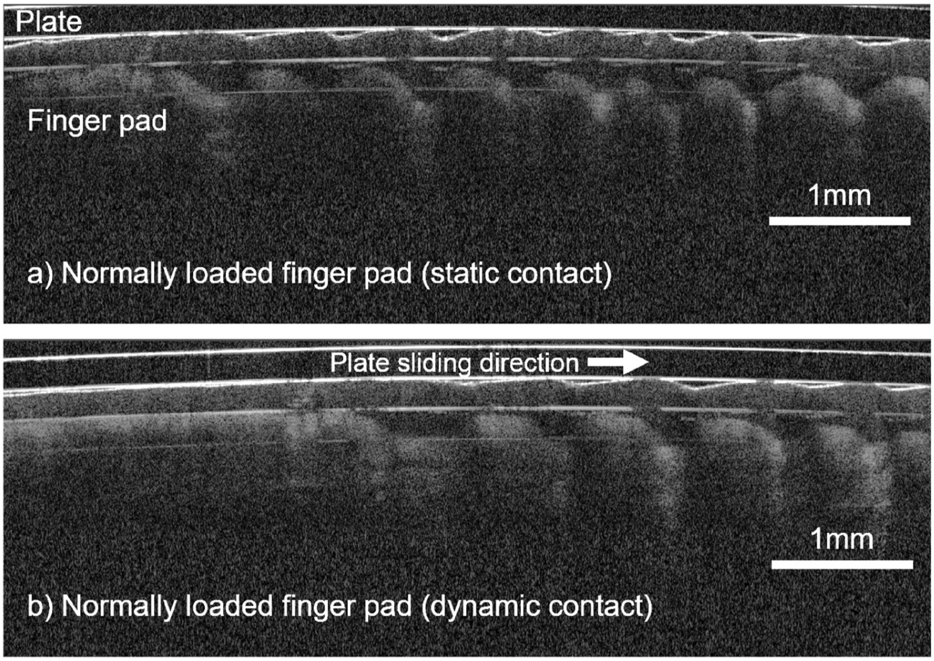

FIGURE 14 | OCT image of a normally loaded finger pad in (a) static condition and (b) dynamic condition.

subsurface tissue deformation and elevated contact pressure. Mean first principal strain (ε_1) rises linearly, whereas mean second principal strain (ε_2) increases rapidly then saturates, mirroring friction's load dependence.

However, this study is constrained to surface strains as subsurface strain measurements (via OCT) were unavailable. Human skin's multilayered viscoelastic structure likely concentrates major deformations subsurface, where tissue recruitment dominates. Nevertheless, surface strains scale systematically with load across static and dynamic conditions, validating them as potential parameter for modelling human finger pad mechanics.

4.6 | Strain Versus Mechanoreceptor Location

Building on the load-dependent strain-friction coupling observed above, dynamic loading redistributes surface strains towards the fingertip, where mechanoreceptor density peaks (see Figure 15). This concentration enhances tactile sensitivity ("feel") during sliding contact as strains align with neural feedback hotspots.

Studying these strain distributions is critical for validating synthetic finger pad models against human biomechanics. The findings guide friction-optimised designs for surfaces and objects, directing interactions to the most sensitive finger pad regions for improved grip perception and control.

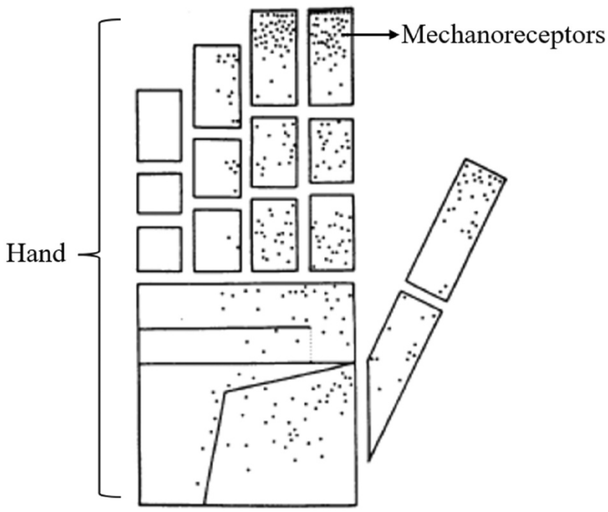

FIGURE 15 | Locations of receptive field centres of 334 glabrous skin mechanoreceptive units. Reproduced from ref. [26]. Tactile sensibility in the human hand: relative and absolute densities of four types of mechanoreceptive units in glabrous skin. Journal of Physiology, vol. 286, pp. 283–300. https://doi.org/10.1113/jphysiol.1979.sp012619 with permission from John Wiley & Sons Inc. (License No. 6204720475717).

4.7 | Measuring the Apparent Contact Area and Real-Apparent Contact Ratio

Apparent contact areas and real-apparent contact area ratio were extracted from 3D-DIC and OCT, respectively. Each modality has distinct limitations: 3D-DIC lacks resolution to resolve fingerprint ridges, whereas OCT captures submacroscopic details but not the full macroscopic contact patch. Combining both provides comprehensive multiscale contact characterisation.

OCT excels for stationary contact area studies, quantifying real and apparent areas via stacked 3D image scans. Dynamic real-time 3D scanning proved infeasible due to motion blur from low scanning speeds IN relative to sliding velocity. Instead, single cross-sectional OCT images (6 mm wide) enabled real-time subsurface monitoring, allowing estimation of real-to-apparent contact area ratios, but not direct measurement.

4.8 | Contact Area Discrepancies

Contact areas in this study were extensively compared with Liu et al. [20], revealing two key discrepancies.

Unlike Liu et al. [20], where dynamic apparent contact area consistently decreased relative to static conditions, the static and dynamic trends appear visually comparable across low loads in this study. This difference likely arises from counterface properties. The thin optical glass substrate exhibited bending even at low loads (see Section 3.1), enabling conformal contact that minimised finger pad viscoelastic deformation during sliding. This could also explain why the surface strain is lower in this study relative to Delhaye et al. [1]. In contrast, Liu et al. [20] used a thick rigid plate (lacking the observed normal load curvature), which promoted lateral subsurface finger pad tissue stretching and contact area shrinkage. This also highlights a limitation of OCT imaging, which cannot capture real-time 3D lateral deformations.

Secondly, static real-apparent contact ratios at low loads were substantially higher in this study than in Liu et al. [20]. Multiple factors likely contribute, including temperature, humidity, skin hydration, subject age and gender. Direct comparison is challenging given single-subject designs in both studies and unreported environmental conditions. Critically, despite comparable static apparent contact areas in both studies, real-apparent ratios differed markedly between subjects, underscoring the variability of fingerprint ridge patterns and the need for real-time large-scale real contact area measurement techniques.

5 | Conclusion

3D-DIC and OCT successfully quantified finger pad deformation-friction interplay during low-load glass sliding, revealing load-driven strain escalation and dynamic fingertip concentration aligning with tactile hotspots. Surface ε_1 scales linearly with normal force whereas ε_2 saturates, mirroring adhesion-dominated friction (CoF 0.4–0.8). Although methodological constraints, such as utilising only single subject surface-only strains and no dynamic OCT 3D scans, limit generalisation, this study still establish proof-of-concept for strain-based human finger pad friction modelling.

These findings advance biomechanics validation for soft robotic grippers, emphasising multiscale imaging to capture real contact evolution and subsurface recruitment absent in synthetic simulants. Future multisubject tests at varied speeds/hydration will refine strain-friction relationships for human-like tactile control.

Funding

The authors have nothing to report.

Conflicts of Interest

The authors declare no conflicts of interest.

Data Availability Statement

Data are available on request.

References

1. B. Delhaye, A. Barrea, B. Edin, P. Lefevre, and J.-L. Thonnard, "Surface Skin Measurements of Fingertip Skin Under Shearing," *Journal of The Royal Society Interface* 13, no. 115 (2016), https://doi.org/10.1098/rsif.2015.0874.

2. B. P. Delhaye, F. Schiltz, F. Crevecoeur, J.-L. Thonnard, and P. Lefèvre, "Fast Grip Force Adaptation to Friction Relies on Localized Finger Pad Strains," *Science Advances* 10, no. 3 (2024): eadh9344, https://doi.org/10.1126/sciadv.adh9344.

3. M. Egawa, M. Oquiri, T. Kuwahara, and M. Takahashi, "Effect of Exposure of Human Skin to a Dry Environment," *Skin Research and Technology* 8, no. 4 (2002): 212–218, https://doi.org/10.1034/j.1600-0846.2002.00351.x.

4. S. E. Tomlinson, M. J. Carre, R. Lewis, and S. E. Franklin, "Human Finger Contact With Small, Triangular Ridged Surfaces," *Wear* 271, no. 9–10 (2011): 2346–2353, https://doi.org/10.1016/j.wear.2010.12.055.

5. S. E. Tomlinson, R. Lewis, X. Liu, C. Texier, and M. J. Carre, "Understanding the Friction Mechanisms Between the Human Finger and Flat Contacting Surfaces in Moist Conditions," *Tribology Letters* 41, no. 1 (2011): 283–294, https://doi.org/10.1007/s11249-010-9709-y.

6. M. J. Adams, S. A. Johnson, P. Lefèvre, et al., "Finger Pad Friction and Its Role in Grip and Touch," *Journal of The Royal Society Interface* 10, no. 80 (2013): 20120467, https://doi.org/10.1098/rsif.2012.0467.

7. S. Derler and L.-C. Gerhardt, "Tribology of Skin: Review and Analysis of Experimental Results for the Friction Coefficient of Human Skin," *Tribology Letters* 45, no. 1 (2012): 1–27, https://doi.org/10.1007/s11249-011-9854-y.

8. X. Liu, Z. Lu, R. Lewis, M. J. Carre, and S. J. Matcher, "Feasibility of Using Optical Coherence Tomography to Study the Influence of Skin Structure on Finger Friction," *Tribology International* 63 (2013): 34–44, https://doi.org/10.1016/j.triboint.2012.08.020.

9. L. J. Wolfram, "Friction of Skin," *Journal of the Society of Cosmetic Chemists* 34 (1983): 465–476, https://doi.org/10.1007/978-3-642-13202-5_5.

10. S. A. Johnson, D. M. Gorman, M. J. Adams, and B. J. Briscoe, "The Friction and Lubrication of Human Stratum Corneum," in *Leeds-Lyon Symposium on Tribology* (Elsevier Science Publishers) (1993), 663–672.

11. M. J. Adams, B. J. Briscoe, and S. A. Johnson, "Friction and Lubrication of Human Skin," *Tribology Letters* 26, no. 3 (2007): 239–253, https://doi.org/10.1007/s11249-007-9206-0.

12. Y. Li, X. Zhou, P. Bai, et al., "Experiment and Modelling of Texture and Sliding Direction Dependence on Finger Friction Behaviour," *Friction* 12, no. 9 (2024): 1955–1968, https://doi.org/10.1007/s40544-023-0816-9.

13. Y. Nakanishi, N. Fujita, K. Miyamoto, D. Morimoto, and R. Suzuki, "Friction and Tactile Sensation of Index Finger Skin on Textured Glass Surfaces During Swipe Motion," *Tribology Letters* 73, no. 2 (2025): 63, https://doi.org/10.1007/s11249-025-01997-y.

14. X. Zhou, M. A. Masen, J. Mo, X. Shi, Y. He, and Z. Jin, "Investigation of Experimental Devices for Finger Active and Passive Tactile Friction Analysis," *Chinese Journal of Mechanical Engineering* 36, no. 1 (2023): 38, https://doi.org/10.1186/s10033-023-00854-0.

15. Z. S. Lee, R. Maiti, M. J. Carré, and R. Lewis, "The Effect of Stiffness on Friction, Surface Strain and Contact Area of a Sliding Finger Pad Simulant," *Tribology Letters* 72, no. 2 (2024): 58, https://doi.org/10.1007/s11249-024-01861-5.

16. P. Reu, "Hidden Components of DIC: Calibration and Shape Function—Part 1," *Experimental Techniques* 36, no. 2 (2012): 3–5, https://doi.org/10.1111/j.1747-1567.2012.00821.x.

17. P. Reu, "Introduction to Digital Image Correlation: Best Practices and Applications," *Experimental Techniques* 36, no. 1 (2012): 3–4, https://doi.org/10.1111/j.1747-1567.2011.00798.x.

18. R. Maiti, L.-C. Gerhardt, Z. S. Lee, et al., "In Vivo Measurement of Skin Surface Strain and Sub-Surface Layer Deformation Induced by Natural Tissue Stretching," *Journal of the Mechanical Behavior of Biomedical Materials* 62 (2016): 556–569, https://doi.org/10.1016/j.jmbbm.2016.05.035.

19. M. F. Kraus, B. Potsaid, M. A. Mayer, et al., "Motion Correction in Optical Coherence Tomography Volumes on a Per A-Scan Basis Using Orthogonal Scan Patterns," *Biomedical Optics Express* 3, no. 6 (2012): 1182–1199, https://doi.org/10.1364/boe.3.001182.

20. X. Liu, M. J. Carre, Q. Zhang, Z. Lu, S. J. Matcher, and R. Lewis, "Measuring Contact Area in a Sliding Human Finger-Pad Contact," *Skin Research and Technology* 24 (2017): 1–14, https://doi.org/10.1111/srt.12387.

21. S. E. Tomlinson, R. Lewis, and M. J. Carre, "The Effect of Normal Force and Roughness on Friction in Human Finger Contact," *Wear* 267, no. 5–8 (2009): 1311–1318, https://doi.org/10.1016/j.wear.2008.12.084.

22. S. Derler, L.-C. Gerhardt, A. Lenz, E. Bertaux, and M. Hadad, "Friction of Human Skin Against Smooth and Rough Glass as a Function of the Contact Pressure," *Tribology International* 42, no. 11–12 (2009): 1565–1574, https://doi.org/10.1016/j.triboint.2008.11.009.

23. A. B. Cua, K.-P. Wilhelm, and H. I. Maibach, "Frictional Properties of Human Skin: Relation to Age, Sex and Anatomical Region, Stratum Corneum Hydration and Transepidermal Water Loss," *British Journal of Dermatology* 123, no. 4 (1990): 473–479, https://doi.org/10.1111/j.1365-2133.1990.tb01452.x.

24. M. Djaghloul, F. Morizot, and H. Zahouani, "Elastic Wave Induced by Friction as a Signature of Human Skin Ageing and Gender Effect," *Skin Research and Technology* (2015).

25. V. H. P. Infante, M. Fehlberg, S. Saikumar, K. Drewing, M. C. Meinke, and R. Bennewitz, "The Role of Skin Hydration, Skin Deformability, and Age in Tactile Friction and Perception of Materials," *Scientific Reports* 15, no. 1 (2025): 9935, https://doi.org/10.1038/s41598-025-95052-4.

26. R. S. Johansson and A. B. Vallbo, "Tactile Sensibility in the Human Hand: Relative and Absolute Densities of Four Types of Mechanoreceptive Units in Glabrous Skin," *Journal of Physiology* 286, no. 1 (1979): 283–300, https://doi.org/10.1113/jphysiol.1979.sp012619.